

Chapter 2

Nanocomposite Films for Wear Resistance Applications

Manish Roy

2.1 Introduction

A new generation thin films which consists of at least two separate phases with one being nanocrystalline or amorphous phase are termed as nanocomposite coatings. These coatings are usually made from ternary or higher order systems and comprise at least two immiscible phases. The most widely studied nanocomposite coatings are ternary, quaternary or even more complex systems having nanocrystalline grains of hard transition metal nitrides (e.g. TiN, AlN, CrN, ZrN, Bn, etc.), carbides (e.g. VC, WC, ZrC, TiC, etc.), borides (e.g. WB, ZrB₂, TiB₂, CrB₂, VB₂, etc.), oxides (e.g. Al₂O₃, TiO₂, Y₂O₃, ZrO₂, etc.) or silicides (e.g. TiSi₂, CrSi₂, ZrSi₂, etc.) surrounding by amorphous matrices (e.g. Si₃N₂, BN, C, etc.). According to Veprék et al., the nanocrystalline grains should be 5–10 nm in size and separated by 2–5 nm within an amorphous phase [1].

These coatings exhibit enhanced mechanical [2–5], physical [6, 7] and functional [8–11] properties. These enhanced properties are due to large interface and nanoscale effects associated with nanocomposite coatings. In these coatings a large volume fraction of atoms are located in the interface where their behaviour is different from the bulk and crystalline size is smaller than 100 nm. There are many fundamental processes in solids that are associated with length scales of around a few nanometres. In recent times, nanocomposite coatings have attracted attention from researchers due to enormous possibilities of synthesising different varieties of nanocomposite films.

The interest in nanocomposite coating has got impetus due to the fact PVD and CVD systems that are used for deposition of coating, leads to the formation of layers having grain sizes much smaller than that obtained by conventional routes.

M. Roy (✉)

Defence Metallurgical Research Laboratory, Kanchanbagh, Hyderabad 500058,
Andhra Pradesh, India
e-mail: rmanish64@rediffmail.com

Further, many of the difficulties for processing the nanocrystalline materials can easily be overcome by these deposition techniques. Vast development of instrumentation techniques allows more precise control of microstructural features and mechanical properties. The possibility to carry out in situ indentation and tribological experiments for both structural and chemical information has propelled design and development of novel coatings in the field of surface engineering.

This chapter reviews the state of art of nanocomposite thin film and their tribological performances and applications. Although it is possible to produce nanocomposite coatings using thermal spray technique, the discussion in this chapter is confined to nanocomposite thin film obtained by CVD or PVD techniques. Thermal spray nanocomposite coatings are discussed in Chap. 1.

2.2 Deposition of Nanocomposite Films

As mentioned earlier, nanocomposite films are usually comprised of minimum two phases, a nanocrystalline phase surrounded by two amorphous phases. Thus synthesis of such coatings depends primarily on co-deposition of both nanocrystalline and amorphous phases such as nc-TiN and nc-TiS₂/a-Si₃N₄ [12], nc-TiB₂/BN [13], nc-TiAlN/a-Si₃N₄ [14], nc-TiC/a-C [15], W₂N/a-Si₃N₄ [16], nc-WC/a-C [17], etc. There are varieties of methods available for deposition of nanocomposite films. The most popular among these methods are plasma-assisted physical vapour deposition (PAPVD) [18], ion-beam and magnetron sputtering [19, 20], combined PVD and PACVD process [1] and also by hybrid process such as magnetron sputtering and laser ablation [21]. However, most widely used method for industrial purpose is magnetron sputtering [22] since this method can be scaled easily for industrial applications and deposition in this method takes place at low temperature. Moreover, any kind of materials can be used as target materials in this method.

Chemical vapour deposition (CVD) technique is another promising method to deposit nanocomposite coatings [23, 24]. Ease of uniform deposition on complicated geometries and fast deposition rate are main advantages of CVD techniques. However, the precursor gases TiCl₄, SiCl₄ and SiH₄ pose main problem due to their corrosive and fire hazardous nature. The deposition temperature for CVD method is relatively high and thus prevents use of such method in many applications. Further, because of presence of chloride, the protective coating may not withstand high temperature exposure for desired duration.

Plasma-enhanced chemical vapour deposition (PECVD) is also known as glow discharge method. The common PECVD method used at lower pressure such as DC or RF discharges operate at pressure of 10–100 mTorr. In RF-PECVD system, electron and ion densities are at most 10¹¹ cm⁻³ at a pressure of 0.1 Torr in which the number density of molecules is of the order of 10¹⁵ cm⁻³. Finger et al. [25] employed very high frequency chemical vapour deposition technique (VHF-CVD) to deposit nanocomposite Si films. Such technique results in increase in deposition rate. Use of hot wire (HW) CVD resulted very good quality nanocomposite films [26, 27]. In this deposition method evaporation of the tungsten filament is a problem

due to high temperature used and this gives rise to contamination. In this method problems can come due to fragile tungsten filament and there can be inhomogeneity when large area is coated.

Electron cyclotron resonance (ECR) CVD system has attracted interest for low temperature deposition of nanocomposite films [28]. In this system, the energy of the electrons in the plasma can be controlled independent of the generation of the damaging ion species. The formation of higher radical particles which deteriorate the film quality is considerably suppressed and highly crystallised films can be grown at 120 °C by ECR-CVD. Electron cyclotron wave resonance (ECWR) CVD provides better coupling to the plasma. This permits use of this system for large area deposition.

Cathodic arc evaporation (CAE) has been used for production of wear resistance coatings [29], coatings for cutting tools [30] and coatings for automotive applications [31] for more than a decade. This process is extremely versatile due to high deposition rate, high degree of ionisation of evaporation species and high ion energies (20–120 eV). However, only materials having good electroconductivity, reasonable mechanical strength and optimum melting point can be used as target material. Many of these problems can be overcome in sputtering process. The main drawback of sputtering process is low degree of ionisation. This drawback has been overcome by introduction of unbalanced magnetron sputtering (UBM) [22] and high power pulsed magnetron sputtering (HPPMS) [32].

In DC magnetron sputtering, a glow discharge is created by applying negative voltage to the target material under vacuum in low pressure inert gas. The application of magnetic field behind target material allows higher deposition rate during sputtering [33]. The development of unbalanced magnetron sputtering has significantly increased the plasma generation area away from the target [34]. The development of closed field unbalanced magnetron sputtering resulted in much higher ion current densities [34]. One of the most important improvements of magnetron sputtering is reactive deposition of ceramic and compound coatings. However, deposition of insulating materials results in deposition of insulating layer on the anode giving rise to ‘disappearing anode’ and deposition of insulating film on target giving rise to ‘poisoned target’. In order to overcome this problem, radio frequency sputtering (RF) was developed. However, RF sputtering suffers from the setback of low deposition rate, high cost and generation of high temperature. In view of the above, in recent times, pulsed DC magnetron sputtering has been developed. During the normal pulse-on-period, the negative sputtering voltage is applied to the target as in conventional DC sputtering. The target negative potential is periodically interrupted by a positive pulse voltage. In the closed field configuration, two or more magnetrons are used in reactive sputtering. All of them can be run in pulsating mode making different combination of mode. Magnetron potential can be pulsed either in asynchronous bipolar mode or in synchronous bipolar mode giving more variation of deposition conditions. In these deposition techniques a high density plasma is created.

Recently high power pulsed magnetron sputtering in unipolar mode has become widely popular. High density plasma is created in front of the sputtering source by using pulsed high target power density, ionising a large fraction of the sputtered

atoms [35]. It is reported that the fraction of ionised species in high power pulsed DC magnetron sputtering can be increased beyond 70 % [36]. This high degree of ionised ions with high energy allows controlling film growth behaviour and thereby produces high quality films. In recent times several nanocomposite coatings are deposited using hybrid coating system where cathodic arc evaporation system is combined with magnetron sputtering technique.

2.3 Important Features of Nanocomposite Films

2.3.1 Microstructural Features of Nanocomposite Films

The main objective of microstructural study of nanocomposite coatings is to determine the structure property relationship so that the gap between atomic structure and the macroscopic properties can be bridged. The most important step in this connection is to ascertain the appropriate length scale where relevant processes take place and the physical basis for such assessment. Although much information can be derived in relation to interfaces because of advent of high resolution transmission electron microscopy (HRTEM), the necessary chemical information at an atomic level is still missing. Field ion microscopy-imaging atom probe is the most important tool for acquiring such information, although other techniques such as an ultrahigh resolution FEG transmission electron microscopy with energy dispersive spectrometry having smaller than 0.5-nm diameter probe can also reveal this information. It can be stated that electron microscopy characterisation accompanied with complimentary techniques serve as a crucial input for deeper understanding for correlating quantitative electron microscopy information to coating properties.

SEM images showing the evolution of the cross-section morphology of W–S–C nanocomposite coatings with increasing C content obtained by reactive sputtering is presented in Fig. 2.1. As can be stated, there is a progressive densification of the coatings with a significant decrease of the number of pores, which results in a decrease of the exposed surface area where O can be adsorbed. With increase in carbon content the film becomes amorphous. The microstructural feature of a nCTiC/a-C:H film deposited using unbalanced magnetron sputter deposition (UMSD) is narrated below. Selected area diffraction (SAD) patterns of four representative samples merged clockwise with decreasing Ti concentration are illustrated in Fig. 2.2 [38]. Diffraction rings point out randomly oriented polycrystalline structure. The upper left diffraction pattern is consistent with hexagonal close-packed lattice of a Ti phase (lattice constants 0.295 and 0.468 nm) with main reflections of the (101), (120), (122) planes. The next pattern in the clockwise direction exhibits that the structure changes with low C content. Simulation of diffraction patterns indicates cubic TiC with lattice constant 0.43 nm and main reflections in the pattern corresponding to (111), (002), (202), (222) planes. The diffraction pattern remains unchanged with increasing C content but becomes more diffuse from about 40 at.% C concentration (sample T303) as TiC nanocrystal grain

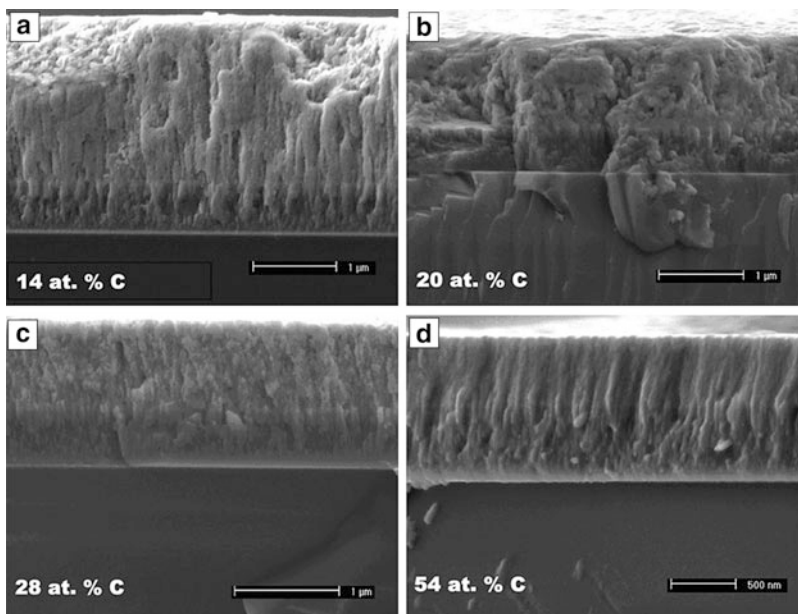


Fig. 2.1 SEM images of a series of W-S-C films containing WC nanograins in the matrix of WS₂ films [37]

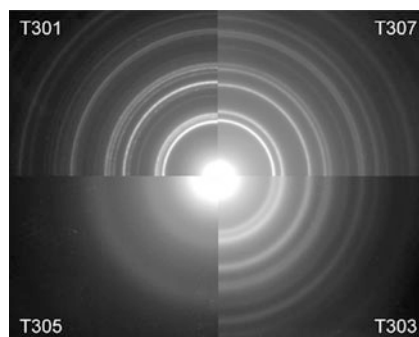


Fig. 2.2 Selected area diffraction (SAD) patterns of four representative samples of a nCTiC/a-C:H film deposited using unbalanced magnetron sputter deposition (UMSD) (clockwise with decreasing Ti concentration) [38]

size decreases and gradually more amorphous a-C:H phase islands are embedded in the TiC phase. At very low Ti concentration (sample T305), no structure was observed in SAD. The highly diffused diffraction pattern corresponds to a-C:H matrix with a decreasing amount of tiny TiC nanocrystals dispersed. Above results correlate well with decreasing grain size in bright field and dark field micrographs as illustrated in Fig. 2.3. TEM images confirm nanometre range grain size.

The XRD patterns of a series of W-S-C films containing WC nanograins in the matrix of WS₂ films are illustrated in Fig. 2.4. The main points worth mentioning

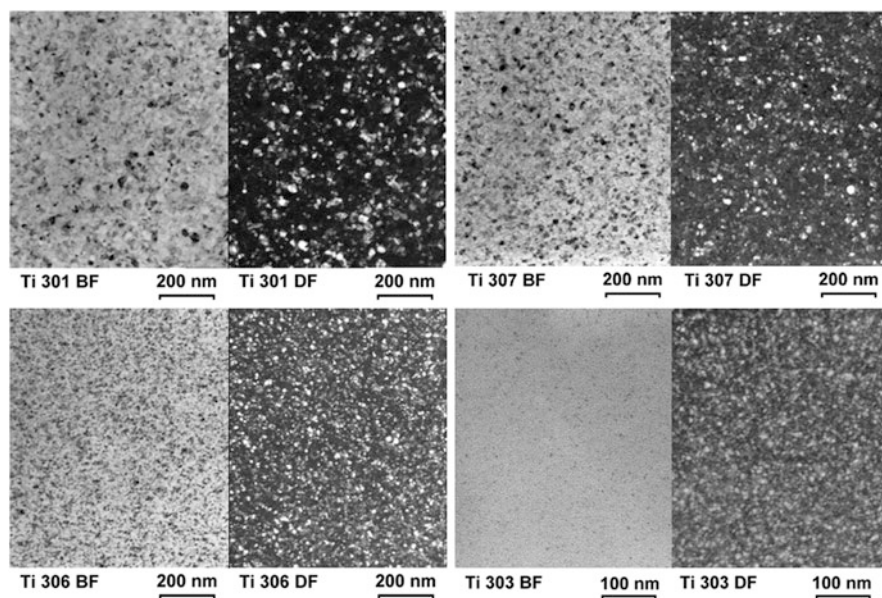


Fig. 2.3 The *bright field* and *dark field* TEM micrographs of a nCTiC/a-C:H film deposited using unbalanced magnetron sputter deposition (UMSD) (with decreasing Ti concentration) [38]

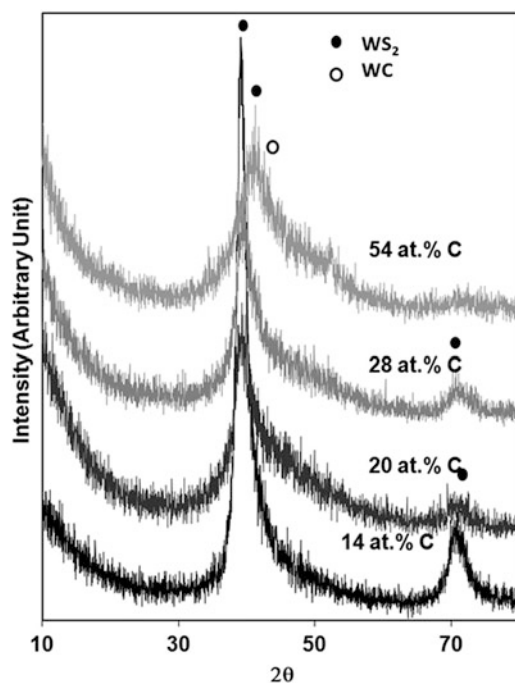


Fig. 2.4 The XRD patterns of a series of W-S-C films containing WC nanograins in the matrix of WS_2 films [37]

are domination of the XRD patterns by main broad asymmetric peaks which are indexed with the general form $(10L)$ corresponding to a turbostratic stacking of the family of plans $(10L)$ with $L = 0,1,2,3$ [39] of the hexagonal WS_2 phase (International Center for Diffraction data (ICDD), Pennsylvania, Card 84-1398; for hexagonal WS_2 also card 841398 is for the same structure); a small peak close to $2\theta \sim 70^\circ$ can be indexed as the (110) plan of WC and a progressive decrease in the crystallinity degree with increasing C content as shown by either the progressive broadening or the decrease in the intensity of the diffraction peaks. It is difficult to detect traces of any other crystalline phase excepting the small features on the right shoulder of the main broad peak which can be related with the presence of a W-C phase. The microstructure of the films can, thus, be described as a nanocomposite consisting of W-S nanocrystals (and in some cases of W-C nanocrystals) embedded in a C-rich amorphous layer.

Raman spectra obtained from similar nanocomposite films obtained by employing different sputtering procedure are presented in Fig. 2.5. All three films show peaks at wave number $1,360\text{ cm}^{-1}$ corresponding to sp^3 bond and another peak at wave number $1,560\text{ cm}^{-1}$. The corresponding bond for pure diamond is at $1,330\text{ cm}^{-1}$. The peak at $1,560\text{ cm}^{-1}$ can be assigned to the G band of microcrystalline graphite. The presence of this band proves existence of sp^2 -bonded carbon within the film. Raman measurement with excitation at 532 nm is much more sensitive to sp^2 carbon than sp^3 carbon. As the peak for G band is more diffused for films obtained by co-sputtering of composite and two targets, than the film obtained by reactive sputtering, presence of more defects can be stated for these films. It is to be stated that no peak corresponding to WO_3 could be noted.

The result of the X-ray photoelectron spectroscopy (XPS) analysis obtained from the W-S-C nanocomposite films having nearly 50 at.% C and obtained by reactive sputtering is presented in Fig. 2.6. It shows the survey spectra after some light Ar sputter cleaning. Peaks for C, S, O, W and N can be noticed. The C peak can be seen at around 285 eV for C-C or C-H bonding, S peak can be seen at around 162 eV binding energy, O peak is obtained at a binding energy around 531 eV and peaks for W can be seen at a binding energy of 35 eV as well as 245, 257 and 425 eV. This is to be stated that WO_3 peak could not be noticed in Raman spectra even though spectra obtained from XPS confirm its presence indicating that oxidation of W is merely a surface-related phenomenon.

2.3.2 Mechanical Properties of Nanocomposite Films

It is already mentioned that nanocomposite coatings exhibit outstanding mechanical properties, in particular, superhardness and excellent tribological properties [40–43]. These outstanding properties are related to nanoscale effects of nanocomposite coatings.

where $H(A)$ is the hardness of pure A and $H(B)$ is the hardness of pure B . a and b are the compositions of A and B in the mixture and $H(A_a B_b)$ is the hardness of the mixture. In coatings with conventional grain size, grain size is one of the ways to increase the hardness. With decrease in grain size, the multiplication and mobility of dislocations are hindered and hardness of the materials increases according to Hall–Petch equation [44, 45].

$$H_d = H_0 + Kd^{-\frac{1}{2}} \quad (2.2)$$

The very high mechanical characteristics [40–43] of nanocomposite coating should be related to specific deformation mechanisms of nanocomposite coatings. It should be stated that the intrinsic deformation mechanisms operating in nanocomposite coatings are similar to that operating in nanocomposite bulk materials. Differences in external factors such as sample geometry, state of stress and substrate effect may change the macroscopic mechanical properties, but intrinsic deformation behaviour remains unchanged. The deformation behaviour of nanocomposite coating is characterised by abnormal Hall–Petch behaviour which manifests itself as either saturation or decrease of yield stress of the coating with decrease of grain size [46, 47]. Under such condition, conventional dislocation slip dominates in nanocomposite coatings having grain size greater than a critical value. Deformation behaviour controlled by active roles of grain boundaries dominate in coatings having very small grain sizes. Although the mechanisms in this regime is not well understood and is a subject of controversy, based on recent literature [48–54], following deformation mechanisms are expected to operate in nanocomposite coatings having grain size less than critical value.

- (a) Lattice dislocation slip
- (b) Grain boundary sliding
- (c) Grain boundary diffusional creep
- (d) Triple junction diffusional creep
- (e) Rotational deformation occurring via movement of grain boundary disclinations
- (f) Twin deformation conducted by partial dislocations emitted from grain boundaries

Lattice dislocation slip is the dominating deformation mechanism in materials having grain size greater than a critical value about 10–30 nm. In nanocomposite coatings, lattice dislocation slip exhibits some specific features owing to interface and nanoscale effects. When the grain size is very small, there is very dislocation for lattice dislocation slip to occur and hence yield stress deviates from classical Hall–Petch relationship. According to some investigators [55, 56] as the particle sizes become smaller, more and more dislocations are absorbed in the grain boundary, leaving low dislocation density and low flow stress. Although there is good correlation between theoretical and experimental data, the question remains that does lattice dislocation exist and play same role in nanocomposite coating as

that of conventional materials? It is pointed out [57] that existence of lattice dislocation is energetically unfavourable in either free nanoparticles or in nanograins.

Grain boundary sliding is caused mainly by grain boundary dislocation having small burgers vector and parallel to grain boundary planes. According to Hahn et al. [58], grain boundary migration is an accommodation mechanism whose combined action with grain boundary sliding gives rise to localization of deformation in nanocomposite coatings. In such case, grain boundary planes become parallel to each other as a result of movement of partial cellular dislocation and defects in arrays of nanograins [59]. In the other case, grain boundary sliding and transformation of defect structures near triple junction of grain boundary result in strengthening. Thus, nanocomposite coatings deformed through grain boundary sliding, either strengthening due to transformation of grain boundary dislocation at triple junctions or softening due to local migration of grain boundary. The competition between strengthening and softening profoundly influences the deformation behaviour of nanocomposite coatings.

Grain boundary diffusional creep or coble creep and triple junction diffusional creep also contribute to plastic flow of nanocomposite coating having very small grains. As the volume fraction of grain boundaries and triple junction phases increases, the importance of these mechanisms in plastic deformation increases. Coatings where grain sizes are very small and thus grain boundary sliding is suppressed, coble creep becomes important deformation mechanism. Some nanocomposite coatings do not contain mobile dislocation grain boundary responsible for grain boundary sliding. In such coatings, coble creep and triple junction diffusional creep are considered important operating mechanism.

Rotational deformation in nanocomposite coating is plastic deformation accompanied by crystal lattice rotation. The main carriers of rotational plastic deformation are believed to be dipoles of grain boundary disinclinations [60]. Grain boundary disinclination is a line defect that separates two grain boundary fragments having different misorientations. Movement of disinclination dipoles causes plastic deformation accompanied by crystal lattice rotation. This mode of deformation is very intensive at times in nanocomposite coatings [61]. The elastic energy of disinclination dipoles diverges rapidly on increasing the distances between disinclinations [62]. Thus dipoles that are close to each other are energetically favourable for grain boundary disinclinations. In nanocomposite coatings, interspacing between neighbouring grains are extremely small. Further, the number of triple junctions where the crossover from conventional grain boundary to rotational deformation occurs is extremely high in nanocomposite coatings.

2.3.2.2 Hardness, Fracture Toughness and Residual Stresses of Nanocomposite Coatings

Hardness of thin films are determined using a nanoindenter equipped with a Berkovich three-sided pyramidal diamond indenter with a nominal angle equal to

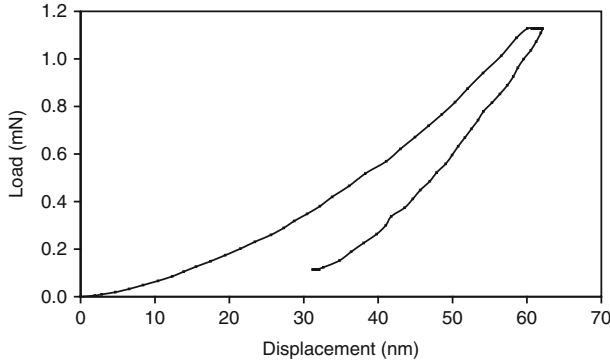


Fig. 2.7 Load vs. displacement diagram obtained for Ti-C:H nanocomposite film

63.5°. In this method, displacement (i.e. penetration depth) is continuously recorded during the total loading and unloading cycle and hence a typical load vs. displacement diagram obtained for Ti-C:H nanocomposite film as presented in Fig. 2.7. The contact depth h_c is estimated from load displacement curve as given below:

$$h_c = h_{\max} - \varepsilon \frac{P_{\max}}{S} \quad (2.3)$$

where h_{\max} is the maximum indentation depth, P_{\max} is the peak indentation load, S is the contact stiffness and ε is a constant which depends on indenter geometry. For Berkovich, $\varepsilon = 0.75$. The contact area A is estimated by evaluating an indenter shape function at contact depth h_c as given below:

$$A = f(h_c) \quad (2.4)$$

The shape function $f(h_c)$ is related to the cross-sectional area of the indenter to the distance from its tip. For the Berkovich indenter, the shape function is given by

$$f(h_c) = 24.56h_c^2 \quad (2.5)$$

Once the contact area is determined from load displacement curve, the hardness is given by

$$H = \frac{P_{\max}}{A} \quad (2.6)$$

The elastic modulus was determined using a procedure enumerated elsewhere [63]. Elastic modulus was calculated employing equation as given below:

$$\frac{1}{E_r} = \frac{(1 - \nu^2)}{E} + \frac{(1 - \nu_i^2)}{E_i} \quad (2.7)$$

and E_r is given by

$$E_r = \frac{0.89S}{\sqrt{A}} \quad (2.8)$$

where S is the slope of the initial part of the unloading curve (in N/m), A is the contact area between the indenter and the substrate (in m^2). E and E_i are the elastic moduli and ν and ν_i are the Poisson ratios of the film and the indenter, respectively. The hardness and elastic modulus of a series of nanocomposite film containing WC grains in WS_2 matrix is presented in Fig. 2.8 [37]. Both the hardness and elastic modulus are improved with increasing at.% of carbon up to a threshold value and then drop down with a further increase of C. The maximum value of the hardness is attained for 54 at.% of carbon, whereas the maximum elastic modulus is noted at 28 at.% of C. As discussed in previous publication [64], such a variation can be attributed to the fact that the film becomes denser with increasing carbon content. Moreover, the possible formation of W-carbide nanograins in coatings with C contents in the range from 40 to 55 at.%, as demonstrated by XPS measurements [64], can justify the maximum of hardness for that value. Once the amount of carbon reaches a saturation point, a further increase in carbon results only in a decrease on the relative amount of W-carbide nanocrystals. This phenomenon is reflected by a decrease of both the hardness and the elastic modulus.

Fracture toughness is another important property for nanocomposite films. According to the theoretical analysis of Li and Bhushan [65], the fracture toughness of nanocomposite film is given by

$$K_{1C} = \left[\left(\frac{E}{(1 - \nu^2)2\pi C_R} \right) \left(\frac{U}{t} \right) \right]^{1/2} \quad (2.9)$$

where E is elastic modulus, ν is Poisson's ratio, $2\pi C_R$ is the crack length in the film plane, U is the strain energy difference before and after cracking and t is the thickness of the film layer. It is well known that the work performed by the indenter during elastic plastic deformation of the film/substrate system is given by the area under the load displacement curve. The strain energy release can be calculated from the loading curve. U is estimated from the peak load of loading and unloading curve. Based on such calculations, the fracture toughness of some films is reported to be between 1.74 and 3.90 $\text{MPa m}^{1/2}$ [66].

The residual stress (σ) of the nanocomposite films are the results of three different types of stresses such as thermal stress (σ_T), growth-induced stress (σ_g) and structure mismatch-induced stress (σ_m) as given below:

$$\sigma = \sigma_T + \sigma_g + \sigma_m \quad (2.10)$$

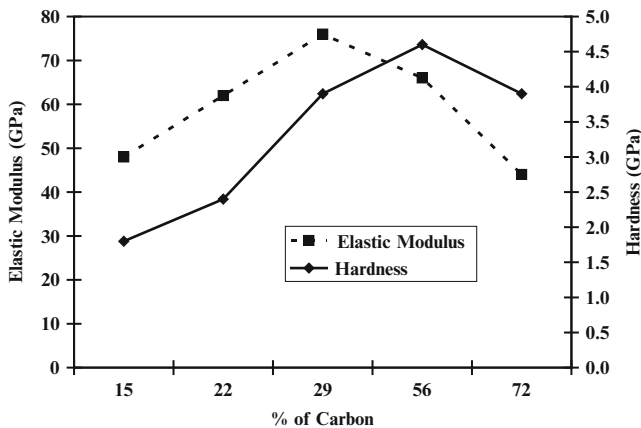


Fig. 2.8 The hardness and elastic modulus of a series of nanocomposite W-S-C film containing WC grains in WS₂ matrix [37]

As most of the nanocomposite films are having amorphous matrix, no stress is generated for matrix mismatch resulting in $\sigma_m = 0$.

Thermal stress is generated due to the mismatch between the CTE of the film and the substrate. Thus the stress in the film due to thermal mismatch can be given as [67, 68]

$$\sigma_T = \frac{E_f}{1 - \nu_f} \int_{T_{\text{dep}}}^{T_{\text{rm}}} (\alpha_s(T) - \alpha_f(T)) dT \quad (2.11)$$

where T_{rm} and T_{dep} are room temperature and deposition temperature, E_f and ν_f are the elastic modulus and Poisson ratio of the film. $\alpha_f(T)$ and $\alpha_s(T)$ are CTE of the film and the substrate respectively.

The growth stress depends on the substrate temperature, gas pressure and kinetic energy of the ions. In general, increase in power density increases the kinetic energy which in turn increases the strain. Increase in power density results in increase in residual stress from 0 to 150 MPa. Sometimes the stress is compressive and sometimes this stress is tensile.

2.4 Tribological Properties of Nanocomposite Films

2.4.1 Friction Behaviour

While engineering the surface of a material for improved performances, attention should be paid in the bulk temperature of the wearing surface. This bulk temperature (T_b) during sliding wear is given as [69, 70]

$$T_b = T_0 + \frac{\alpha \mu F v l_b}{A_n K_m} \quad (2.12)$$

where T_0 is room temperature, α is a constant known as heat distribution coefficient, μ is the friction coefficient, F is applied load, v is sliding velocity, l_b is mean heat diffusion distance, A_n is nominal area of contact and K_m is thermal conductivity of the metal.

The contact temperature at the asperities, known as flash heating temperature is given by [69, 70]

$$T_f = T_b + \frac{\mu v r}{2K_e} \left(\frac{H_o F}{N A_n} \right)^{\frac{1}{2}} \quad (2.13)$$

where H_o is the hardness of the oxide scale, N is the total no of the asperities, r is the radius of the contacting area and K_e is the equivalent thermal conductivity. Other symbols are as above.

From both the equation it is clear that for a given tribological condition, the bulk temperature or the flash temperature is controlled by friction coefficient i.e. these temperatures increase with increase of friction coefficient. If the flash temperature increases beyond some values, the mechanism of wear will change from plasticity-dominated wear to mild oxidational wear. Further if the bulk temperature is high, the hardness of the degrading layer tends to come down leading to increased wear rate in plasticity dominated wear. One way of reducing the temperature is to lower the friction coefficient. In view of these, most nanocomposite films contain an amorphous matrix phase. These amorphous phases are known for their low friction coefficient [71, 72]. This is more so with a-C phase which transform to graphitic structure and helps in reducing friction coefficient by acting as lubricant.

In support of above statement, the observation of Sánchez-López et al. [73] can be presented. Their observation indicates decrease of friction coefficient with increasing volume fraction of amorphous a-C phases. The tribological behaviour of nanocomposite films composed by metallic carbides mixed with amorphous carbon (a-C) was assessed by comparing TiC/a-C, WC/a-C and TiBC/a-C series prepared by magnetron sputtering technique with variable carbon contents. The friction coefficients appear to correlate with the overall carbon content. By estimation of the percentage of carbon atoms situated in the amorphous lubricant phase, a comparative analysis was done in selected samples providing similar friction coefficient (~ 0.2). The Raman analysis of the ball counterfaces demonstrates the formation of a graphitic-like material for the more lubricant films (i.e. those containing higher fraction of a-C) during friction. The relative amount of a-C [xa-C] needed to reduce friction below 0.2 is diminished in the nanocomposite films formed by metastable or non-stoichiometric carbides (TiBC/a-C and WC/a-C) from 55–60 (case of TiC/a-C) to 30–40 %. This decrease was attributed to a partial C release into the contact due to the decomposition or transformation of these compounds under friction. Figure 2.9 plots the evolution of friction coefficients

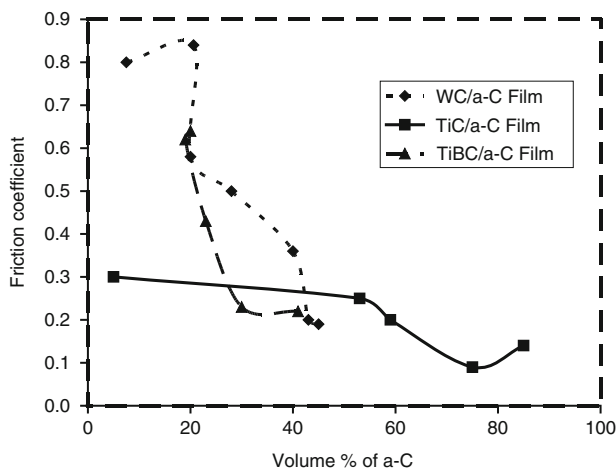


Fig. 2.9 The evolution of friction coefficients with lubricant fraction, xa-C [73]

vs. lubricant fraction, xa-C. The friction coefficient tends to decrease rapidly for the WC/a-C and TiBC/a-C systems from 0.6–0.8 to values below 0.2 for a-C contents above 40 %. For obtaining a similar low friction coefficient with the TiC/a-C nanocomposite films, it is necessary the a-C fraction rises up to 60 %. Further reduction of the friction, even below 0.1, can be achieved by increasing the fraction lubrication to a higher extent but always smaller percentages are needed for the WC/a-C and TiBC/a-C films. Feng et al. [74] deposited Ti-C:H coatings by inductively coupled plasma (ICP)-assisted hybrid chemical vapour deposition-physical vapour deposition (CVD/PVD). These Ti-C:H coatings consist of nanocrystalline TiC clusters embedded in an a-C:H matrix and are thin film TiC_y amorphous hydrocarbon (a-C:H) nanocomposite materials. Results point to the fact that at Ti compositions 20 at.%, the friction coefficients stay relatively constant at 0.1. This low friction coefficient is characteristic of hard carbon-based coatings. At Ti compositions greater than 30 at.%, the friction coefficients are also relatively constant. However, they now show a greater than twofold increase in the friction coefficient to 0.25. A friction coefficient in this range is typical for unlubricated sliding between ceramic materials, such as metal carbides and metal nitrides [75].

A comparative study of nc-TiC/a-C(Al) coatings (C₅₆Ti₃₁Al₁₃) and nc-TiC/a-C coating (C₆₄Ti₃₆) was carried out against 100Cr6 steel balls. It was noted that the friction coefficient of nc-TiC/a-C(Al) coatings is lower than the friction coefficient of nc-TiC/a-C coating in spite of having lower a-C content as nc-TiC/a-C coating was harder and rougher than nc-TiC/a-C(Al) coatings. The friction coefficients of these nanocomposite coatings are higher than that of pure a-C coatings due to presence of less amount of graphitic phase and high hardness. However, friction coefficients of these nanocomposite coatings are lower than that of currently used industrial coatings such as TiN, CrN, TiC, etc. [76–81]. Similar observation related to lower friction coefficient of nanocomposite coatings due to presence of

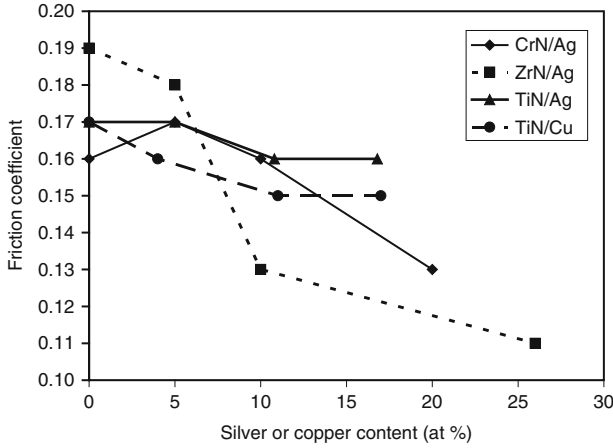


Fig. 2.10 Variation of friction coefficient as function of Ag or Cu content of a series of CrN/Ag, ZrN/Ag, TiN/Ag, TiN/Cu nanocomposite coatings deposited using dual pulsed magnetron sputtering system [83]

amorphous a-C phase and decrease of friction coefficient as a result of increase of amorphous a-C phase is also noted by Lindquist et al. [82] and Stuber et al. [83]

Another reason for reduction of friction coefficient is increase of elastic modulus and hardness of these coating. The increase in elastic modulus and hardness results in decrease of the plowing component of the friction force as per given equation [84]:

$$\mu_P = C \frac{K_{IC}^2}{E\sqrt{HN}} \quad (2.14)$$

where C is a constant, K_{IC} is fracture toughness for mode one fracture, E is elastic modulus, H is hardness and N is normal load. Kelly et al. [85] deposited CrN/Ag, ZrN/Ag, TiN/Ag and TiN/Cu nanocomposite coatings using dual-pulsed magnetron sputtering system. These coatings were subjected to unlubricated thrust washer wear testing [86] against 100Cr6 steel washer at ambient condition at an rpm of 30 at applied load of 100 N. This kind of test provides conformable geometry that is encountered in mechanical seal, pumps and sideways. Their results are shown in Fig. 2.10. The friction coefficient varies between 0.16 and 0.19, this reduced friction coefficient is attributed to enhanced film growth condition obtained due to pulsed DC mode [87]. Further the friction coefficient was found to decrease with increasing silver or copper content. The largest reduction is obtained for the film ZrN/Ag which decreased from 0.19 to 0.11 at 25.9 % Ag primarily due to increase of hardness and elastic modulus as described in Eq. (2.14).

Cheng et al. [88] deposited TiSiN nanocomposite coatings with a thickness of 2.5 μm using a large area filtered arc deposition (LAFAD) technique with TiSi targets having different Si content. The tribological behaviours of the TiSiN

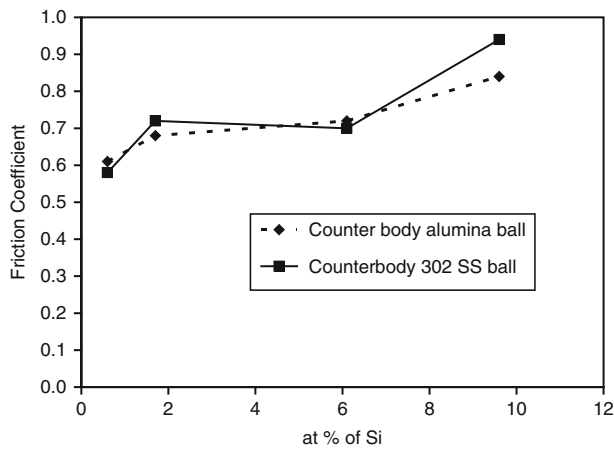


Fig. 2.11 Variation of friction coefficient with Si content of TiSiN coating against Al_2O_3 and 302 SS ball as counterbody [88]

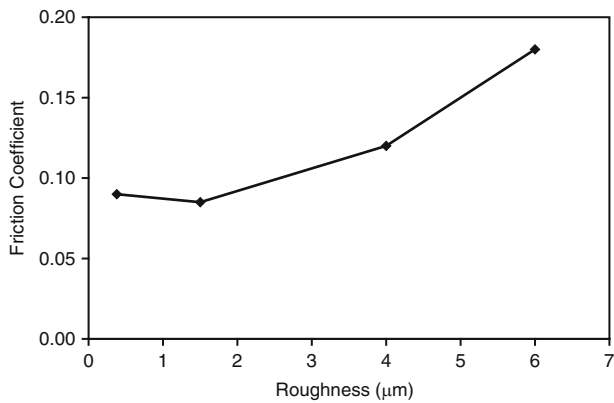


Fig. 2.12 The influence of roughness on the friction coefficient of nanocomposite TiC/a-C coating [89]

coatings are strongly dependent on the Si content in the coatings and the testing ball material. TiSiN coatings exhibit similar friction coefficient when tested against Al_2O_3 and 302 stainless steel balls as shown in Fig. 2.11. However, increase of Si content causes an increase in the friction coefficient of the TiSiN coatings. With the increase in the Si content in the coatings, the wear rate of the TiSiN coatings decreases when tested against Al_2O_3 balls, but increases significantly when tested against 302 stainless steel balls. The capability of forming a transfer layer on the ball surface contributes to the change in the friction coefficient and wear rate with Si content in the coating and ball materials.

Roughness is an important parameter that governs the friction coefficient. The work due to Shaha et al. [89] is presented in Fig. 2.12. They deposited TiC/a-C film

by simultaneous DC sputtering of Ti and pulsed DC sputtering of graphite. Their work exhibits increase of friction coefficient with increasing roughness. The increase of friction coefficient with increasing roughness is in line with the mechanism proposed by earlier investigator [90, 91]. Higher roughness increases the asperities slope angle which in turn increases friction coefficient [90]. Thus the ratcheting mechanism where relative motion between two surfaces is achieved by asperities riding over each other is responsible for increase of friction coefficient. The second possible mechanism related to energy loss mechanism where asperities push each other also holds good here

Yttria-stabilized zirconia (YSZ) has a unique combination of mechanical properties. Young's modulus and thermal expansion coefficient of this material are close to metals. Hardness is 11–15 GPa. Fracture toughness is one of the highest among oxide ceramics. They have excellent thermal stability [92]. The tribological properties of YSZ have been intensely studied [93–95]. At high contact loads, the friction coefficient quickly increases (over a period of a few hundred cycles) to 0.6–1.2 due to the accumulation and entrapment of hard wear debris, causing abrasive wear [96]. Wear and friction mechanisms of thin YSZ coatings have not been investigated very intensely [97–99]. A common problem reported for these coatings is brittle fracture in friction contacts due to substrate compliance and coating residual stress [100]. One of the most successful uses of YSZ protective coatings has been as 20–50-nm overcoats on magnetic recording media [101]. Voevodin et al. [102] improved the friction performances of YSZ film by adding gold, making the film a nanocomposite, where hard and brittle nanograins of YSZ were surrounded by amorphous gold matrix. Their observation is illustrated in Fig. 2.13. As can be seen from Fig. 2.13 that addition of 10 % Au results in nanocomposite structure which in turn helps in reducing the friction coefficient to as low as 0.2 even at 773 K suppressing abrasion wear as commonly observed in YSZ coatings.

In addition, a large variety of nanocomposite films exhibited outstanding tribological properties. An excellent antiwear performance is reported by Wang et al. [103] for CrAlN nanocomposite films with various Al contents prepared by a reactive magnetron sputtering technique using Cr and Al targets in the reactive gas mixture. Scharf et al. [104] noted that Co-sputtering at room temperature with any amount of Ti induced a dramatic change in the microstructure. Ti prevented the formation of crystalline WS_2 , making it amorphous with well-dispersed nanocrystalline (1–3 nm) precipitates. A longer thin film lifetime was exhibited when the thin films were doped with low amounts of Ti (5–14 at.%) in comparison to pure WS_2 , but there was no change in friction coefficient (0.1). According to Low et al. [105], nanocomposite nickel coatings reinforced with regularly shaped nanotubular titanates (multilayered wall structure with 5 nm internal diameter and 30–500 nm tube length), electrodeposited from a modified Watts nickel electrolyte have shown (1) 22 % reduction in surface friction against a spherical diamond tip, (2) 29 % enhancement in wear resistance in a three-body slurry abrasive wear test (steel counter body and 5 μ m SiC particles), when compared with a nickel coating containing irregularly shaped nanosized titanium dioxide particles. Ma et al. [106]

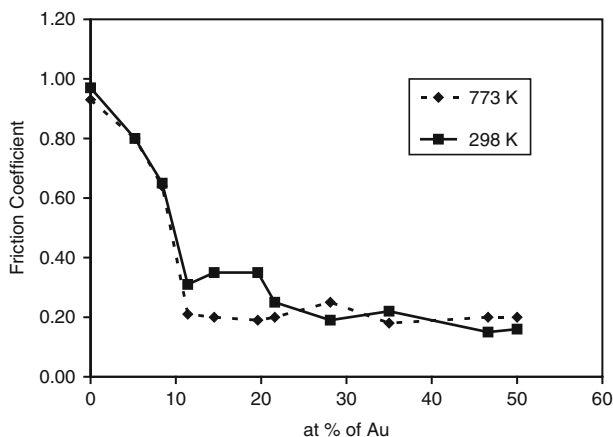


Fig. 2.13 The effect of Au content on the friction coefficient of YSZ nanocomposite film containing gold [100]

studied a series of quaternary Ti–Si–C–N nanocomposite coatings deposited on HSS substrate at 823 K using a pulsed direct circuit plasma-enhanced chemical vapour deposition (PECVD) equipment with a gas mixture of $\text{TiCl}_4/\text{SiCl}_4/\text{H}_2/\text{N}_2/\text{CH}_4/\text{Ar}$. The results show that the nanocomposite Ti–Si–C–N coatings with low Si and high C contents have a lower friction coefficient of 0.17–0.35 at room temperature. The Ti–Si–C–N nanocomposite coating containing 12 at.% Si and 30 at.% C shows excellent tribological properties with a low friction coefficient of 0.30 and a low wear rate at 773 K. Neidhardt et al. [107] successfully synthesised wear-resistant Ti–B–N nanocomposite coatings by reactive arc evaporation from partially metallic Ti/TiB₂ cathodes. Higher N₂ fractions in this film result in a thermodynamically stable nanocrystalline TiN phase embedded in an amorphous BN matrix. The amount of boundary phase can be adjusted with the Ti/B ratio of the cathodes. At lower N₂ partial pressures, a TiN–TiB_x structure is observed, with strong indications for a substitutional solid solution of B in TiN, giving rise to a maximum in hardness (>40 GPa) and wear resistance regardless the Ti/B ratio in the cathodes. All coatings show coefficients of friction of 0.7 ± 0.1 against alumina balls. The dry wear behaviours of reactive unbalanced dc-magnetron sputtered Ti–B–N thin films deposited on silicon (100) at room temperature were investigated by Lu et al. [108]. Both friction coefficient and specific wear rate decreased with incorporation of B into TiN or increasing B content. With increasing applied load, the friction coefficient increased. However the specific wear rate exhibited an inverse trend, accompanying with an increase in amount of deformed wear debris. Increasing sliding velocity yielded similar results to those of increasing loading, which might be due to strain rate effect. Oxygen of H₂O in air participated in and reacted with films and formed mainly Ti oxide consisting of TiO, TiO₂ and Ti₂O₃, accompanying with minor amount of FeO in debris. The formation of oxide in debris was believed to have an effect on increasing wear resistance.

Nanocomposite TiBCN coatings with different nitrogen contents were synthesised by sputtering a TiBC (80 mol.% TiB_2 to 20 mol.% TiC) compound target in various Ar/N_2 mixtures by Lin et al. [109]. When the nitrogen content was less than 5 at.%, the coatings were characterised as a mixture of nano-columnar grains of the $\text{Ti}(\text{B},\text{C})$ crystalline phase embedded in a small fraction of amorphous-free carbon and CN. These coatings exhibited superhardness (>45 GPa), but poor adhesion, toughness and wear resistance due to the prominent TiB_2 -type structure and the deficiency of a sufficient amorphous phase. When the nitrogen content was increased to 8–15 at.%, the substitution of N for B atoms in the $\text{Ti}(\text{B},\text{C})$ lattice led to a gradual decrease in the $\text{Ti}(\text{B},\text{C})$ phase and an increase in the volume fraction of the $\text{Ti}(\text{N},\text{C})$ and amorphous BN phases. The microstructure of these coatings was characterised as nanocrystalline solid solution $\text{Ti}(\text{B},\text{C})$ and $\text{Ti}(\text{N},\text{C})$ compounds embedded in an amorphous BN, free carbon and CN matrix. These coatings showed a slight decrease in the coating hardness (37–45 GPa), but significant improvements in the adhesion and wear resistance. However, excessive incorporation of N into the TiBCN coatings (>20 at.%) resulted in a great reduction of the hard $\text{Ti}(\text{B},\text{C})$ phase accompanied with the formation of a large volume fraction of amorphous BN, which resulted in a decrease in both hardness and wear resistance.

Friction coefficient can be reduced if it is possible to increase the number of slip systems available for deformation. This can be achieved by adding Si to some systems. Addition of Si results change of orientation of surfaces, increasing the number of available slip system and also formation of amorphous phase a-SiN giving rise to lower friction coefficient. Both phenomena result in reduction of friction coefficient. Pilloud et al. [110] reduced the friction coefficient of ZrN film by adding Si on it. Zr–Si–N films have been deposited on steel and silicon substrates using a reactive magnetron process. ZrN coatings exhibit a [111] preferred orientation, whereas Zr–Si–N ones with low silicon content (<5.7 at.%) exhibit a [100] preferred orientation. Furthermore, the nanocomposite films grow with a columnar structure and their roughness decreases when the silicon content increases. The resultant nanocomposite film exhibits reduced friction coefficient. Friction tests conducted against steel and alumina balls show that the Zr–Si–N films do not suffer any wear when sliding against steel. Only material transfer from the ball onto the film has been detected. When the alumina ball was used, the coatings suffer an significant wear except the amorphous film containing the highest amount of silicon (7.6 at.%).

Similarly ZrN and ZrN–Ag films were deposited using reactive unbalanced magnetron sputtering by Aouadi et al. [111]. The films formed a microstructure that consisted of dense and homogeneous nanocrystals of Me evenly distributed throughout the ZrN matrix. The films became more textured with the (111) preferred orientation for larger substrate bias. Nanoscratch tests suggested that the films with the largest silver content had the lowest wear rate probably because of the high pressures associated with these measurements. Wear testing using the more conventional ball-on-disc technique indicated improvements in the tribological properties of the films that may be correlated to the improvements in the resistance to plastic deformation established from nanoindentation measurements. Overall,

nanoindentation, nanowear, and ball-on-disc techniques proved that ZrN–Ag films had superior mechanical properties than ZrN. Further, Cr–Si–N coatings with a nanocomposite microstructure were deposited using closed unbalanced magnetron sputtering ion plating system by Bao et al. [112]. The hardness and modulus of Si-doped Cr–N coatings have been improved with the rise of Si concentrations. The improvement of hardness of Cr–Si–N coatings is attributed to both solid solution strengthening and higher density of the doped coatings. Si-doped Cr–N coatings have a lower friction coefficient which is due to the non-crystal Si compounds with a low friction coefficient.

2.4.2 Wear Behaviour

In recent time, it is demonstrated that not only hardness or elastic modulus but also the ratio H/E is a very important material property [113]. The ratio H/E multiplied by geometric factor, which is ratio of the diameter of plastic zone to total deformed zone, gives the plasticity index. The plasticity index describes the deformation properties of contacting surfaces. This quantity also appears in various expressions for fracture toughness. It was recognised by several authors that the ranking of materials according to their H/E ratio can provide extremely close agreement to their ranking in terms of wear [114]. Various authors have accepted that the H/E ratio as a ranking parameter since Oberle's early study [115, 116].

The support of above hypothesis can be found in the work of Lin et al. [109] as given in Fig. 2.14. TiBCN nanocomposite coatings were deposited in a closed field unbalanced magnetron sputtering system using pulsed magnetron sputtering of a TiBC compound target with various Ar/N₂ mixtures. Improvements in the coating adhesion, H/E ratio and wear resistance were achieved together with a decrease in the coating hardness to 35–45 GPa as the N content in the coatings was increased from 8 to 15 at.%. The microstructure of the coatings changed from a nanocolumnar to a nanocomposite structure in which 5–8 nm nanocrystalline Ti(B,C) and Ti(N,C) compounds were embedded in an amorphous matrix consisting of BN, free carbon and CN phases. With a further increase in the N content in the coatings to levels greater than 20 at.%, the inter-particle spacing of the nanocrystalline compounds increased significantly due to the formation of a large amount of the amorphous BN phase, which also led to low hardness and poor wear resistance of the TiBCN coatings.

The Ti–Al–B–N phase system offers a broad range of possibilities for designing coating structures with optimal properties for different applications. Further, the addition of aluminium to TiN/TiB₂-based nanocomposite structure provides scope for lowering the elastic modulus of the coating (E_{Al} —70 GPa). The presence of boron allows the possibility to produce a soft, low-modulus (and potentially dry-lubricant) h-BN phase, superhard (or ultrahard) and stiff c-BN or an amorphous phase, depending on the deposition conditions [117–119]. Furthermore, the 'doping' of titanium-based vapour-source materials with several atomic percent

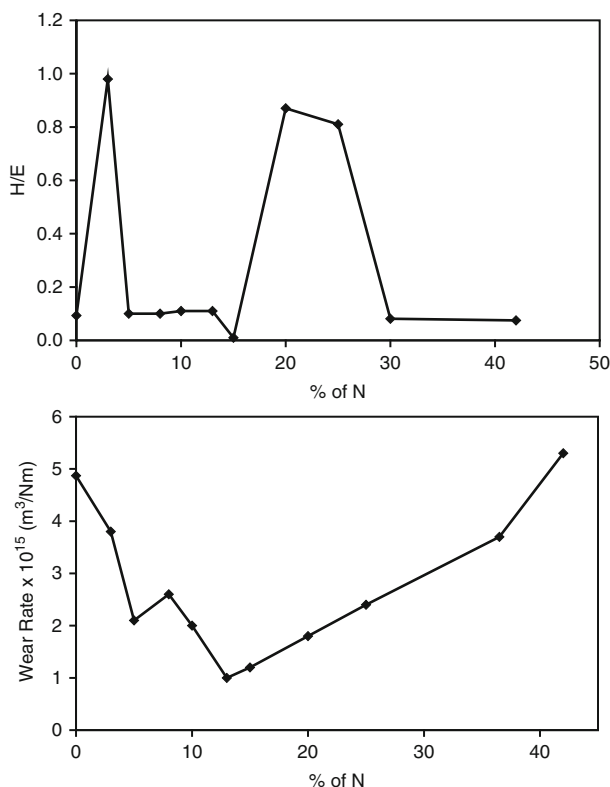


Fig. 2.14 Variation of H/E ratio and wear resistance of TiBCN nanocomposite coating as function of nitrogen content [109]

of boron can be used to produce a nanocrystalline material with very similar hardness and elastic properties to those of tool steel, which makes an excellent metallic interlayer for ceramic coatings [120]. The incorporation of 2–3 at.% B into a TiN film creates a coating which is significantly harder (i.e. >30 GPa) than ‘conventional’ TiN and exhibits dramatically reduced sliding wear [119]. The use of interstitial doping to create metallic coatings which has lower elastic moduli than most ceramic coatings and are hard and wear resistant, has been observed in systems other than Ti–Al–B–N (e.g. W–C [121] and Cr–N [122]), with distinct benefits in each case.

There exist two main practices for the production of nanocomposite coatings. In one of the practices, the nanocomposite structure is obtained by the combination of two hard and immiscible phases in one coating (e.g. nc-TiN/a-Si₃N₄; a-TiSi₂-nc-TiSi₂) while in the other practice, the mixture of one hard and one soft immiscible phases (e.g. Zr–Cu–N, Cr–N–Cu, Ti–Cu–N and Mo–Cu–N) are used. Nanocomposite coatings based on hard/hard phases has been extensively studied [123–126]. Less attention has been paid to those composite coatings that are based

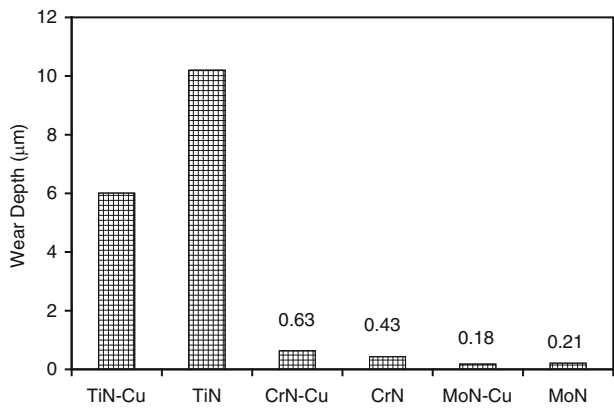


Fig. 2.15 Wear depth of various nanocomposite coatings showing the beneficial effect of Cu addition in improving wear [127]

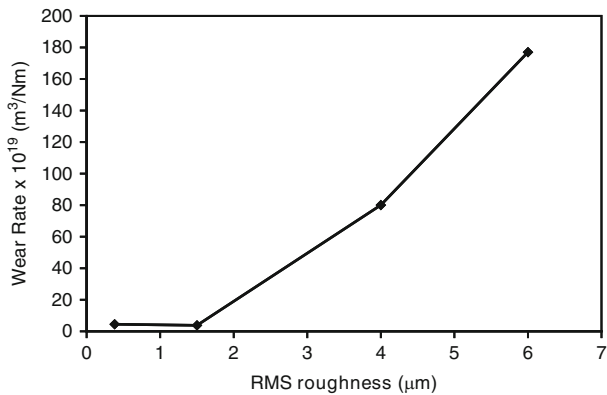


Fig. 2.16 The influence of roughness on wear rate of TiC/a-C coating [89]

on hard/soft phases. Ozturk et al. [127] investigate tribological behaviours of Cu-doped TiN, CrN, and MoN coatings using hard soft phase combination. The results of their investigation confirmed that the addition of Cu into TiN, CrN and MoN coatings has indeed modified the grain size and morphology, but beneficial effect is experienced only on the friction and wear behaviour of MoN. Their results are shown in Fig. 2.15. Similar to the case of friction coefficient, the wear rate also increases with increase of surface roughness as can be shown in Fig. 2.16 by Shaha et al. [89].

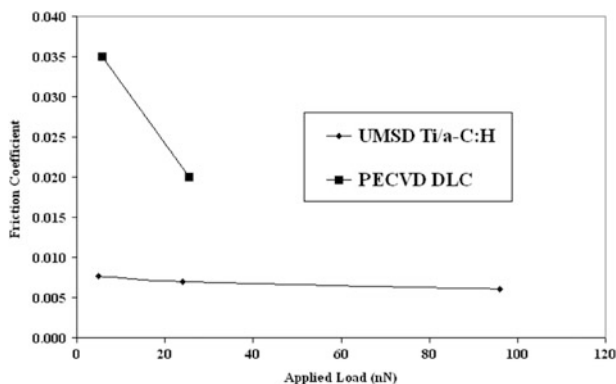


Fig. 2.17 The effect of applied load on the friction coefficient of Ti/a-C:H nanocomposite and DLC film [38]

2.4.3 Nanotribology

The possibilities of using these coatings for tribological applications at low load such as for microelectromechanical system, micromechanical assembly, etc. are explored [71, 128]. Work due to Kvasnica et al. [38] on tribology of n-TiC/a-C nanocomposite film at nN load is presented in Fig. 2.17. It is noted that the friction coefficient is independent of scan speed and applied load in this load range for n-TiC/a-C nanocomposite film. In a separate study by Koch et al. [37], using constant load scratch indenter, it is noted that the friction coefficient of W-S-C nanocomposite film decreases with increase of carbon content. Their observation is presented in Fig. 2.18. WS₂ has an excellent friction behaviour in dry atmospheres contrary to humidity containing ones. Some kinds of C-phases behave in reverse way. Thus, when testing in ambient condition, the coatings rich in C-phases exhibit lower friction coefficient than the others with lower C content. Further such behaviour specially the friction behaviour at very low load may also be attributed to presence of oxygen in the film. Oxygen either in adsorbed state or by forming a thin complex layer increases the friction coefficient. The problem of the humidity in W-S-C system is the fact that O can establish strong bonds between the basal planes impeding the easy sliding and increasing the friction coefficient. Of course if one increases the porosity, the surface where O/H₂O can be adsorbed is increased facilitating the establishment of these bonds. Both porosity and the tendency to react with O₂ increases with decreasing carbon content in these films. This results in lower friction coefficient at higher carbon content. Further, it is also found that the friction coefficients exhibit a maximum value at the lowest applied load. Such behaviour is clearly related to the fact that at lower applied load the friction is powerfully governed by the surface forces. Furthermore, the friction coefficient also increases with the sliding distance. As the scratch tip moves along the surface, the material scratched out piles up in the front of the tip, giving rise to

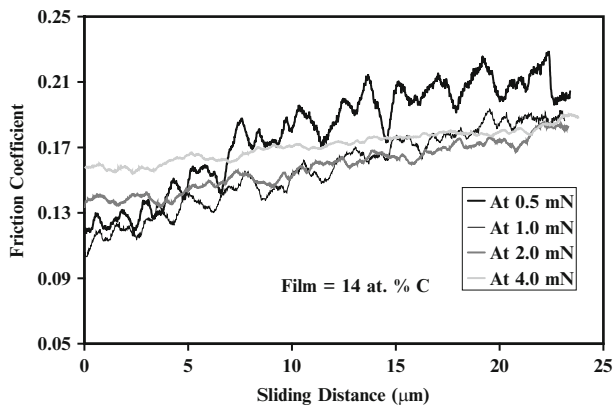


Fig. 2.18 Variation of friction coefficient with sliding distance for W-S-C film containing 14 at. % C [37]

an enhanced resistance to the motion of the tip and hence a higher friction force is realised. Further, it is reported that during sliding in WS_2 system, propagation of pre-existing cracks breaks covalent bonds creating more unsaturated bonds [129]. When sliding takes place in ambient condition, such unsaturated bonds react with the moisture in air forming WO_3 . The formation of WO_3 tends to increase the friction force.

Finally, it is to be stated that the scratch test is mostly concerned with scratching a specimen with a V-shaped indenter in general a diamond indenter. Such scratching simulates an ideal single contact abrasive process. However, such a single asperity contact has several shortcomings. Single asperity contact does not simulate possible mechanical interlocking between asperities. Such experiment also fails to simulate the distribution of loads over several asperities as encountered in practical applications. On the other hand self-lubricating films are used mostly in sliding wear applications. The state of stress and the thermodynamic nature of the deformation of the material under an abrasive process or a sliding process differ considerably. For example, the strain rate during abrasive wear is around $1-10 \text{ s}^{-1}$ whereas the strain rate during sliding wear is around 10^{-2} to 1 s^{-1} . During abrasive wear, material deformation is constrained and partially adiabatic [130]. In contrast, during sliding wear, material deformation is characterised by constrained isothermal deformation. Thus friction study using a microtribometre with ball-on-disc configuration simulates ideal sliding wear conditions. It is possible to cover the entire contact area uniformly with carbonaceous graphitic material during scratching. This may not take place during reciprocating sliding action.

In order to overcome the above-mentioned shortcomings, low load tribological study is carried out for n-TiC/a-C nanocomposite film. The effect of the stroke length on the friction coefficient of such film at 500 mN load is shown in Fig. 2.19 [131]. Clearly the friction coefficient reaches a minimum at 500 μm stroke length. The highest friction coefficient is noted for 1,000 μm stroke length. Friction

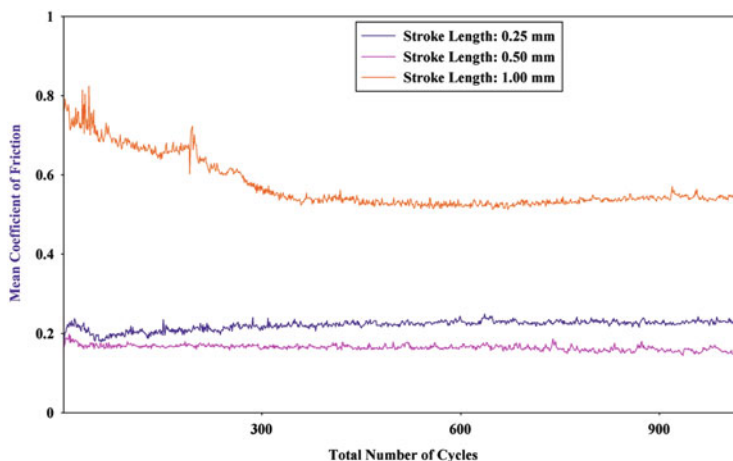


Fig. 2.19 The effect of the stroke length on the friction coefficient of such film at 500 mN load of TiC/a-C film [137]

coefficients for 500 and 250 μm stroke length remain constant through out the test. The friction coefficient at 1,000 μm stroke length decreases from an initial high value and attains a constant value.

The friction force is found to be minimum at an intermediate stroke length. The friction coefficient is very high at higher stroke length of 1,000 μm . As the frequency of reciprocation (0.8 Hz) remains constant, the average velocity of the interacting surfaces increases with increase in stroke length. This results in increase of temperature at the contact point giving rise to the formation of a higher amount of oxide debris. This oxide debris subsequently acts as an abrasive giving rise to higher friction coefficients at higher stroke length. It is also noted that the friction coefficient at higher stroke length decreases from an initial high value to a low constant value. This may be attributed to the fact that the contact temperature during reciprocating motion with high stroke length is high. Hence carbon tends to get graphitised as the process of wear continues and the friction coefficient decreases. After some time the friction coefficient goes down and the contact temperature does not attain a high enough value to allow graphitisation to take place. Consequently the friction coefficient does not decrease further but rather assumes a steady state value. The above observation can also be related to the fact that as the sliding continues, the real contact area increases, resulting in a decrease of the mean pressure and consequently ploughing action decreases.

Topographic images obtained using SPM from the worn surfaces of W–S–C nanocomposite films obtained by employing different sputtering procedure and rubbed against 52100 steel ball at very low load are illustrated in Fig. 2.20. In all films, extensive ploughing can be noted. This ploughing forces the material to the ridges along the sides of the grooves. These displaced material subsequently chipped out leading to material loss. These grooves are due to ploughing action

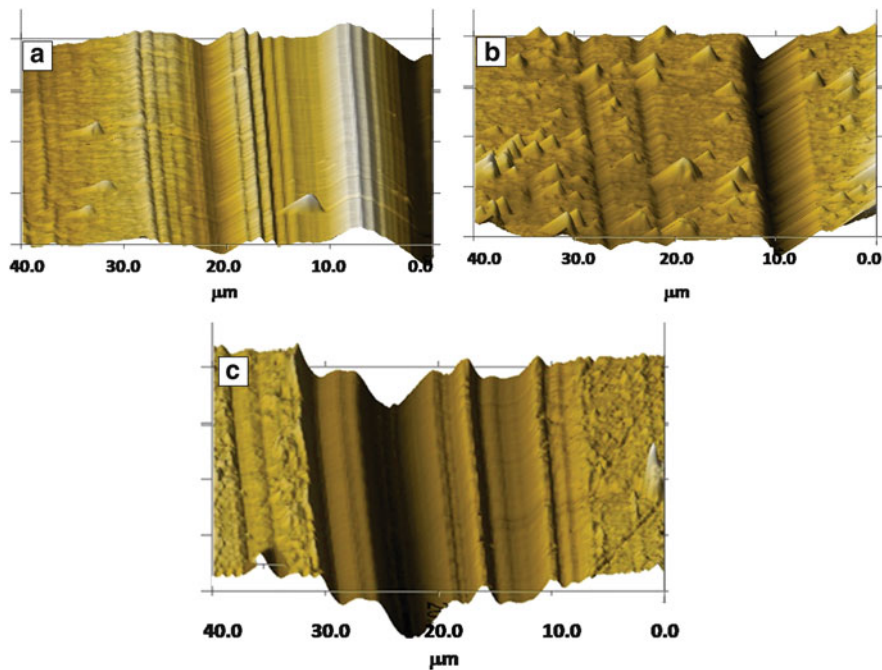


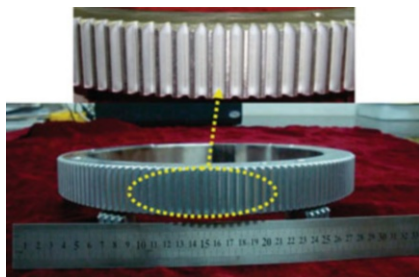
Fig. 2.20 Topographic images obtained using SPM from the worn surfaces of W-S-C films obtained by employing different sputtering procedure and rubbed against 52100 steel ball at very low load, (a) reactively sputtered, (b) co-sputter with two different target and (c) co-sputter with composite target

of the asperities. Within the wear track, the depth and width of the grooves varied from place to place and from films to films.

2.5 Applications of Nanocomposite Films

Piston ring of internal combustion engine is considered to be a potential area for application of nanocomposite nc-TiC/a-C(Al) film [132]. Pure a-C film is not considered for such application as high residual stress prevents thick film to be deposited. Thickness below 1.5 μm or even a few microns does not meet the requirement of acceptable mileage. Further pure a-C coating exhibits poor thermal stability, oxidation resistance and brittle behaviour. In contrast, the important features of nc-TiC/a-C(Al) film indicated that this will be excellent coating for such application. The low residual stresses of the film allow thicker coating to be deposited. The piston ring of a two-stroke gasoline engine having capacity 41 cc, cylinder bore of 39.8 mm and stroke of 32.55 mm is coated with nc-TiC/a-C(Al) film. The piston ring is 1.65-mm thick, having inside diameter of 36.32 mm and

Fig. 2.21 Image of CrAlN coated gears with a film thickness of approximately 15 μm [132]



outside diameter of 39.37 mm. The engine test is carried out for 610 h. It is noted that with nc-TiC/a-C(Al) film, wear of the coating is considerably lower and around 3 % fuel is saved in first 30 h and 2 % fuel is saved in next 580 h.

As mentioned earlier, nanocomposite films are considered as potential protective surfaces for moving parts such as gears, cutting tools and shafts used in engines or other industries to replace the traditional CrN films. Such kinds of nanocomposite films have now been successfully deposited on large-scale gears (nearly 300 mm in diameter, stainless steel AISI 304) used in polishing machines [133]. Figure 2.21 shows the whole picture of CrAlN-coated gears with a film thickness of approximately 15 μm . It can be clearly observed that the coated tooth surface of gears is very uniform, smooth and compact. In addition, the CrAlN films exhibited very excellent bonding with the gears. The servicing life and failure process of such nanocomposite CrAlN-coated gears are found to improve significantly. Images of several components such as turbine blades, cutting tools, etc. coated with nanocomposite film (Dextron Research Ltd., Russia) using UniCoat 600 and UniCoat 700 systems are given in Fig. 2.22.

The nanocomposite nc-($\text{Al}_{1-x}\text{Ti}_x$)N/a- Si_3N_4 film is developed for the purpose of metal cutting operation [134, 135]. The cutting performance of this coating in dry and minimum lubrication condition is 2–4 times better than the state-of-the-art ($\text{Al}_{1-x}\text{Ti}_x$)N coating. During dry drilling of tough steel, the life time of drill bits made of cemented carbide coated with this film is four times higher than that coated with state-of-the-art ($\text{Al}_{1-x}\text{Ti}_x$)N coating [136, 137].

Fox et al. [138] reported MoS_2/Ti composite coating by co-deposition of small amount Ti in MoS_2 matrix. The properties of this coating are available elsewhere [139]. Drilling tests were carried out. High-speed steel M6 tap drills have been coated with TiN, TiCN (low carbon content), TiAlN (high aluminium content), TiN + MoS_2 /Titanium composite and TiCN (low carbon content) + MoS_2 /titanium composite. These tap drills were tested under dry conditions and lubricated (mixed oil and water soluble by 20 %) condition to drill 5.5 mm through holes into AISI 400 stainless steel (11.7 mm thick, HRB 60–70). These tests were performed at 530 rpm and at 1,061 rpm. The number of holes produced was recorded. Use of MoS_2 /titanium composite in dry conditions on the top of hard coatings such as TiN and TiCN has increased the number of holes produced by twice in the case of TiN and by 4.1–4.8 times for TiCN [140]. Carbide end mills have been coated with



Fig. 2.22 Images of several components coated with nanocomposite film (Dextron Research Ltd., Russia)

TiCN and TiCN + MoS₂/titanium composite and were tested. These end mills were tested under dry conditions and lubricated (Trim Sol: mixed oil and water-soluble by 5 %) at a cutting speed of 150 m/min and a feed rate of 0.04 mm/turn onto AISI 304 stainless steel. The cutting depth was 4 mm, while the radial depth cut was 3 mm and the axial depth cut was 5 mm. Average milling force, tool wear and surface finishing were recorded. It has also been observed that MoS₂/titanium composite coatings running in dry conditions deposited on top of a TiCN hard coating offer an increase in milling distance and a reduction in average milling force during the test and improvement of surface finish [140]. Punches were coated with MoS₂/titanium composite (1.2 μm) on top of TiCN (3–3.5 μm of TiCN produced by arc evaporation) coating and used to perforate 12 mm HSLA steel with water soluble lubricant (20 %). In the piercing application, an uncoated tool was able to pierce 15,000 parts before tool failure. The use of a TiCN coating increased the number of parts to 50,000 and depositing MoS₂/titanium composite on top of TiCN further increased the number of parts to 200,000 [140].

2.6 Summary and Perspectives

In this chapter, the state of art of the research of nanocomposite coatings and their tribological performances is reviewed. Over the last decade, significant efforts are being put for research and development of nanocomposite coatings and this has yielded wealth of information on structure property relation and tribological performances of these coatings. There is a growing interest in nanocomposite wear-resistant coating, in particular, transition metal nitrides with increased thermal stability because of their wide spread applications. These coatings are finding other

applications such as nuclear fuel materials, diffusion barrier, laser diodes electrical contacts, etc.

The generic concept of design of super hard nanocomposite coatings is based on spinodal phase segregation resulting in formation of stable nanostructure by self organisation. The deformation behaviour of nanocomposite coatings is having typical features controlled by interfaces and nanoscale effects in these coatings. For tribological performances the ratio of hardness to elastic modulus of the coating has been proved to be an important property. These nanocomposite coatings lend themselves to incorporate 'adaptive' and 'chameleon'-type attributes.

One important challenge for nanocrystalline coating is to develop a process which can produce nanocomposite coating with controlled grain size, shape, crystallographic orientation and lattice structure. Such nanocomposite coatings are expected to have enhanced optical, electrical, magnetic, electronic and photocatalytic properties.

Doping of oxides by metal is expected to produce new generation nanocomposite coating with self-healing functionality. Considerable effort has been provided to produce TiO_2 -based film with photocatalytic, self-healing, antifogging and antibacterial properties [141, 142]. The present research is concerned with doping this film with an element in order to shift activation of these properties from ultraviolet to visible light region by forming a nanocomposite coating.

Industrial applications of nanocomposite coatings expose them to elevated temperature and oxygen. However, detail study on oxidation mechanism is rare although such data will help designing and tailoring the coatings for applied thermal load. Further, research in the area of diffusion related phenomena controlling recovery, recrystallization, segregation, grain growth interdiffusion, etc. are to be investigated in much more detail for development of next generation nanocomposite coatings.

Another important area is to have enhanced understanding of the nonlinear elastic behaviour and mechanism of plastic deformation of nanocomposite coatings. Many nanocomposite coatings are macroscopically brittle but microscopically ductile and this may be due to plastic instability in the material. It is important to understand and control plastic instability of these materials.

References

1. Veprek S, Nesladek P, Niederhofer A, Glatz F, Jilek M, Sima M (1998) *Surf Coat Technol* 108–109:138
2. Veprek S, Reiprich S (1995) *Thin Solid Films* 268:64–71
3. Budrovic Z, Van Swygenhoven H, Derlet PM, Van Petegem S, Schmitt B (2004) *Science* 304:273–276
4. Van Swygenhoven H, Specer M, Caro A (1999) *Acta Mater* 47:3117–3126
5. Provenzano V, Holtz RL (1995) *Mater Sci Eng A* 204:125–134
6. Gleiter H (1989) *Prog Mater Sci* 33:223–315

7. Musil J, Viecek J (2001) *Surf Coat Technol* 142–144:557–566
8. Yip S (1998) *Nature* 391:532–533
9. Mazaleyrat F, Varga LK (2000) *J Magn Magn Mater* 215–216:253–259
10. Gusev AI (1998) *Physics-Uspekhi* 41(1):49–76
11. Maya L, Allen WR, Grover AL, Mabon JC (1995) *J Vac Sci Technol B* 13(2):361–365
12. Veprek S, Niederhofer A, Moto K, Bolom T, Mannling HD, Nesladek P, Dollinger G, Bergmeier A (2000) *Surf Coat Technol* 133–134:52
13. Park IW, Kim KH, Kumrath AO, Zhong D, Moore JJ, Voevodin AA, Levashov EA (2005) *J Vac Sci Technol B* 23(2):588
14. Park IW, Kim KH, Suh JH, Park CG, Lee MH (2003) *J Korean Phys Soc* 42(6):783
15. Roy M, Kvasnica S, Eisenmenger-Stittner C, Vorlauffer G, Pauschitz A (2005) *Surf Eng* 21 (3):257
16. Cavaleiro A, Louro C (2002) *Vacuum* 64(3):211
17. Voevodin AA, O'neil JP, Prasad SV, Zabinski JS (1999) *J Vac Sci Technol A* 17(3):986
18. Veprek S (1999) *J Vac Sci Technol A* 17:1521
19. Musil J (2000) *Surf Coat Technol* 125:322
20. Kelly PJ, Arnell RD (2000) *Vacuum* 56:159
21. Voevodin AA, Zabinski JS (1998) *Diam Relat Mater* 7:463
22. Seo SC, Ingram DC, Richardson HH (1995) *J Vac Sci Technol B* 13(2):2856
23. Safi I (2000) *Surf Coat Technol* 127:203
24. Choy KL (2003) *Prog Mater Sci* 48:57
25. Finger F, Hapke P, Luysberg M, Carius R, Wagner H, Scheib M (1994) *J Appl Phys Lett* 65:2588
26. Alpium P, Chu V, Conde JP (1999) *J Appl Phys* 86:3812
27. Heintze M, Zedlitz R, Wanka HN, Schubert MB (1996) *J Appl Phys* 79:2699
28. Wang KC, Hwang HL, Leong PT, Yew TR (1995) *J Appl Phys* 77:6542
29. Knotek O, Prengel HG (1991) *Surf Modif Technol* 4:507
30. Tanaka Y, Ichimiya N, Onishi Y, Yamada Y (2001) *Surf Coat Technol* 146–147:215
31. Merlo AM (2003) *Surf Coat Technol* 174:21
32. Ehiasarian AP, Hopsipian PE, Hartman L, Helmersson U (2004) *Thin Solid Films* 457:270
33. Kelly PJ, Arnell RD (1998) *Surf Coat Technol* 108–109:317
34. Arnell RD, Kelly PJ (1999) *Surf Coat Technol* 112:170
35. Kouznetsov V, Macak K, Schneider JM, Helmersson U, Petrov I (1999) *Surf Coat Technol* 122:190
36. Ehiasarian AP, New R, Munz WD, Hartman L, Helmersson U, Kouznetsov V (2002) *Vacuum* 65:147
37. Koch T, Pauschitz A, Roy M, Evaristo M, Caveleiro A (2009) *Thin Solid Films* 518:185
38. Kvasnica S, Schalko J, Benardi J, Eisenmenger-Sittner C, Pauschitz A, Roy M (2006) *Diam Relat Mater* 15:1743
39. Regula M, Ballif C, Moser JH, Lévy F (1996) *Thin Solid Films* 280:67
40. Veprek S, Argon AS (2002) *J Vac Sci Technol B* 20:650
41. Patscheider J (2003) *MRS Bull* 28:173
42. Veprek S (2003) *Rev Adv Mater Sci* 5:6
43. Veprek S, Argon AS (2001) *Surf Coat Technol* 146–147:175
44. Hall EO (1951) *Proc Phys Soc Lond Sec B* 64:747
45. Petch NJ (1953) *J Iron Steel Inst* 174:25
46. Mohamed FA, Li Y (2001) *Mater Sci Eng A* 298:1
47. Padmanavan KA (2001) *Mater Sci Eng A* 304:200
48. Ovid'ko A (2002) *Science* 295:2386
49. Ovid'ko A (2005) *Int Mater Rev* 50:65
50. Kim HS, Estrin Y, Bush MB (2000) *Acta Mater* 48:493
51. Liao XZ, Zhao F, Lavernia E, He DW, Zhu YT (2004) *Appl Phys Lett* 84:632
52. Chen MW, Ma E, Hemkar KJ, Sheng HW, Wang YM, Cheng XM (2003) *Science* 300:1275

53. Koch CC (2003) *Scr Mater* 49:657
54. Ovid'ko A (2005) *Rev Adv Mater Sci* 10:89
55. Malygin GA (1995) *Phys Solid State* 37:3
56. Evans AG, Hirth JP (1992) *Scr Metall* 26:1675
57. Romanov AE (1995) *Nanostruct Mater* 6:125
58. Hahn H, Mondal P, Padmanabhan KA (1997) *Nanostruct Mater* 9:603
59. Ovid'ko IA (2003) *Philos Mag Lett* 83:611
60. Seefeldt M (2001) *Rev Adv Mater Sci* 2:44
61. Yu Gutkin M, Ovid'ko IA (2003) *Rev Adv Mater Sci* 4:79
62. Ramanov AE, Valdimirov VI (1992) In: Nabarro FRN (ed) *Dislocations in solids*, vol 9. North Holland Pub, Amsterdam, p 191
63. Oliver WC, Pharr GM (1992) *J Mater Res* 7:1564
64. Nossa A, Cavalerio A (2004) *J Mater Res* 19:2356
65. Li X, Diao D, Bhushan B (1997) *Acta Metall* 45:4453
66. Ding J, Meng Y, Wen S (2000) *Thin Solid Films* 371:178
67. Fu YQ, Du HJ, Sun CQ (2003) *Thin Solid Films* 424:107
68. Slack GA, Bartram SF (1975) *J Appl Phys* 46(1):89
69. Lim SC, Ashby MF (1987) *Acta Metall* 35:11
70. Roy M (2009) *Trans Indian Inst Met* 62:197
71. Roy M, Koch T, Pauschitz A (2010) *Adv Surf Sci* 256:6850
72. Sánchez-López JC, Martínez-Martínez D, López-Cartes C, Fernández A (2008) *Surf Coat Technol* 202:4011
73. Sánchez-López JC, Martínez-Martínez D, Abad MD, Fernández A (2009) *Surf Coat Technol* 204:947
74. Feng B, Cao DM, Meng WJ, Rehn LE, Baldo PM, Doll GL (2001) *Thin Solid Films* 398–399:210
75. Hutchings IM (1992) *Tribology, friction and wear of engineering materials*. CRC, Boca Raton, FL
76. Singer ILS, Fayeulle S, Ehni PD (1991) *Wear* 149:375
77. Myake S, Kaneko R (1992) *Thin Solid Films* 212:256
78. Jamal T, Nimmagadda R, Bunshah RF (1980) *Thin Solid Films* 73:245
79. Zhang S, Bui XL, Li X (2006) *Diam Relat Mater* 15:972
80. Panjan P, Navisek B, Cekada M, Zalar A (1999) *Vacuum* 53:127
81. Zhang S, Fu YQ, Du HJ (2002) *Surf Coat Technol* 162:42
82. Lindquist M, Wilhelmsson O, Jansson U, Wiklund U (2009) *Wear* 266:379
83. Stuber M, Leiste H, Ulrich S, Holleck H, Schild D (2002) *Surf Coat Technol* 150:218
84. Briscoe J, Stolarski TA (1993) In: Glaeser WA (ed) *Friction in characterisation of tribomaterials*. Butterworth-Heinemann, Boston, MA, p 44
85. Kelly PJ, Li H, Benson PS, Whitehead KA, Verran J, Arnell RD, Lordanova I (2010) *Surf Coat Technol* 205:1606
86. Kelly PJ, Li H, Whitehead KA, Verran J, Arnell RD, Lordanova I (2009) *Surf Coat Technol* 204:1137
87. Kelly PJ, von Braucke T, Liu Z, Arnell RD, Doyle ED (2007) *Surf Coat Technol* 202:774
88. Cheng YH, Browne T, Heckerman B, Meletis EI (2010) *Surf Coat Technol* 204:2123
89. Shaha KP, Pei YT, Martinez-Martinez D, De Hosson JTM (2010) *Surf Coat Technol* 205:2624
90. Hayward IP, Singer IL, Seitzman LE (1991) *Wear* 157:215
91. Bull SJ, Chalkar PR, Johnston C, Moore V (1994) *Surf Coat Technol* 68:603
92. Wachtman JB (1996) *Mechanical properties of ceramics*. Wiley, New York, p 161, 392
93. Lancaster JK, Mashal Y, Salher R (1992) *J Phys D* 25:A205
94. Fischer TE, Anderson MP, Jahamir S, Salher R (1988) *Wear* 124:133
95. Stachowiak GW, Stachowiak GB (1989) *Wear* 132:151
96. Lee SW, Hsu SM, Shen MC (1993) *J Am Ceram Soc* 76:1937

97. Kao AS, Hwang C (1990) *J Vac Sci Technol A* 8:3289
98. Dugger MT, Chung YW, Bhushan B, Rothschild W (1993) *Tribol Trans* 36:84
99. Yamashita T, Chen GL, Shir J, Chen T (1988) *IEEE Trans Magn* 24:2629
100. Moulzolf SC, Lad RJ, Blau PJ (1999) *Thin Solid Films* 347:220
101. Theunissen GSAM (1998) *J Mater Sci Lett* 17:1235
102. Voevodin AA, Hu JJ, Fitz TA, Zabinski JS (2001) *Surf Coat Technol* 146–147:351
103. Wang L, Zhang G, Wood RJK, Wang SC, Xue Q (2010) *Surf Coat Technol* 204:1517
104. Scharf TW, Rajendran A, Banerjee R, Sequeda F (1999) *Thin Solid Films* 347:220
105. Low CTJ, Bello JO, Wharton JA, Wood RJK, Stokes KR, Walsh FC (2010) *Surf Coat Technol* 205:1856
106. Ma D, Ma S, Dong H, Xu K, Bell T (2006) *Thin Solid Films* 496:438
107. Neidhardt J, Czigány Z, Sartory B, Tessadri R, Mitterer C (2010) *Int J Refract Met Hard Mater* 28:23
108. Lu YH, Shen YG, Zhou ZF, Li KY (2007) *Wear* 262:1372
109. Lin J, Moore JJ, Mishra B, Pinkas M, Sproul WD (2010) *Acta Mater* 58:1554
110. Pilloud D, Pierson JF, Takadom J (2006) *Thin Solid Films* 496:445
111. Aouadi SM, Bohnhoff A, Sodergren M, Mihut D, Rohde SL, Xu J, Mishra SR (2006) *Surf Coat Technol* 201:418
112. Bao M, Yu L, Xu X, He J, Sun H, Teer DG (2009) *Thin Solid Films* 517:4938
113. Musil J, Jirout M (2007) *Surf Coat Technol* 201:5143
114. Oberle TL (1951) *J Met* 3:438
115. Lancaster JK (1963) *Br J Appl Phys* 14:497
116. Halling J (1982) *Tribologia* 1(2):15
117. Rebholz C, Ziegele H, Leyland A, Matthews A (1998) *J Vac Sci Technol A* 16(5):2851
118. Rebholz C, Schneider JM, Voevodin AA, Steinebrunner J, Charitidis C, Logothetidis S, Leyland A, Matthews A (1999) *Surf Coat Technol* 113:126
119. Rebholz C, Leyland A, Matthews A (1999) *Thin Solid Films* 343–344:242
120. Rebholz C, Leyland A, Larour P, Charitidis C, Logothetidis S, Matthews A (1999) *Surf Coat Technol* 116–119:648
121. Rebholz C, Schneider JM, Leyland A, Matthews A (1999) *Surf Coat Technol* 112:85
122. Rebholz C, Ziegele H, Leyland A, Matthews A (1999) *Surf Coat Technol* 115:222
123. Musil J, Zeman P (1999) *Vacuum* 52:269
124. Abadias G, Tse YY, Michel A, Jaouen C, Jaouen M (2003) *Thin Solid Films* 43:166
125. Musil J, Zeman P, Hruby H, Mayrhofer PH (1999) *Surf Coat Technol* 120–121:179
126. He JL, Setsuhara Y, Shimizu I, Miyake S (2001) *Surf Coat Technol* 137:8
127. Ozturk A, Ezirmik KV, Kazmanlı K, Urgan M, Eryılmaz OL, Erdemir A (2008) *Tribol Int* 41:49
128. Tomala A, Gebeshuber IC, Pauschitz A, Roy M (2010) *Int J Mater Res* 101(7):845–851
129. Prasad S, Zabinski J (1997) *Nature* 387:761
130. Roy M (2006) In: *Proceedings of the international conference on advances in materials and materials processing*, Kharagpur, India, 3–5 Feb, p 202
131. Pauschitz A, Jisa R, Kvasnica S, Bernardi J, Koch T, Roy M (2008) *Diam Relat Mater* 17:2010
132. Zhang S, Bui XL, Sun D (2007) In: Zhang S, Ali N (eds) *Nanocomposite thin films and coatings*. Imperial College, London
133. Wang L, Zhang G, Wood RJK, Wang SC, Xue Q (2010) *Surf Coat Technol* 204:3517
134. Halubar P, Jilek M, Sima M (2000) *Surf Coat Technol* 133–134:145
135. Veprek S, Mannling HD, Jilek M, Halubar P (2004) *Mater Sci Eng A* 366:202
136. Jilek M, Cselle T, Halubar P, Morstein M, Veprek-Heijman MGJ, Veprek S (2004) *Plasma Chem Plasma Process* 24(4):493
137. Cselle T (2003) *Werkzeug Technik* No 77, March 2–7
138. Fox VC, Renevier NM, Teer DG, Hampshire J, Rigato V (1998) In: *Proceedings of the PSE conference*, Garmisch Partenkirchen, 14–18 Sept

139. Teer DG, Hampshire J, Fox V, Bellido-Gonzalez V (1997) *Surf Coat Technol* 94(95):572
140. Renevier NM, Lobiondo N, Fox VC, Teer DG, Hampshire J (2000) *Surf Coat Technol* 123:84
141. Herman JM, Disdier J, Pichat P (1984) *Chem Phys Lett* 108:618
142. Asahi R, Morikawa T, Ohawaki T, Aoki K, Taga Y (2001) *Science* 293:269

Surface Engineering for Enhanced Performance against
Wear

Roy, M. (Ed.)

2013, IX, 319 p., Hardcover

ISBN: 978-3-7091-0100-1